

Surface-Based Manipulation

Ziqiao Wang^{1†}, Serhat Demirtas^{1†}, Fabio Zuliani¹, Jamie Paik^{1*}

¹Swiss Federal Institute of Technology Lausanne (EPFL),
Reconfigurable Robotics Laboratory, Lausanne, 1015, Switzerland.

*Corresponding author(s). E-mail(s): jamie.paik@epfl.ch;
Contributing authors: ziqiao.wang@epfl.ch; serhat.demirtas@epfl.ch;
fabio.zuliani@epfl.ch;

[†]These authors contributed equally to this work.

Abstract

Intelligence lies not only in the brain but in the body. The shape of our bodies can influence how we think and interact with the physical world. In robotics research, interacting with the physical world is crucial as it allows robots to manipulate objects in various real-life scenarios. Conventional robotic manipulation strategies mainly rely on finger-shaped end effectors. However, achieving stable grasps on fragile, deformable, irregularly shaped, or slippery objects is challenging due to difficulties in establishing stable force or geometric constraints.

Here, we present surface-based manipulation strategies that diverge from classical grasping approaches, using with flat surfaces as minimalist end-effectors. By changing the position and orientation of these surfaces, objects can be translated, rotated and even flipped across the surface using closed-loop control strategies. Since this method does not rely on stable grasp, it can adapt to objects of various shapes, sizes, and stiffness levels, even enabling the manipulation the shape of deformable objects. Our results provide a new perspective for solving complex manipulation problems.

1 Introduction

Physical morphologies of a body significantly influence how it interacts with and perceives its environment [1–6]. In nature, many animals have evolved diverse grasping mechanisms to adapt to various contexts—for example, manual grippers resembling anthropomorphic hands [7], spinal grippers such as the prehensile tails of monkeys and certain lizards, and muscular hydrostats like octopus tentacles and elephant trunks [8]. Roboticians draw inspiration from the biological systems to develop grippers that utilize mechanical interlocking for geometric constraints [9–11], friction for force constraints [12–15], or adhesion for stabilization [16–18]. These methods form the basis of most current robotic gripper designs [19, 20]. However, they often face challenges when manipulating irregularly shaped, deformable, or fragile objects [21]. Purely geometric constraints struggle with irregular shapes, and force constraints can damage deformable or delicate items. Reflecting on our daily experiences (see Fig. 1a), we often address similar challenges by adopting surface-based, nonprehensile manipulation methods and providing support from below. For example, while chopsticks are effective for picking up solid foods like fried potatoes, a spoon is more suitable for deformable substances like mashed potatoes. We hold a basketball with our palms rather than gripping it solely with our fingers, and we support a slippery fish from underneath. These examples demonstrate that when traditional grasping is ineffective, we naturally resort to surface-based, nonprehensile manipulation strategies. Motivated by this observation, introducing surface-based end effectors into robotics by adapting their morphology to planar forms offers a promising solution to these challenges.

Robotics research has introduced devices capable of dynamically altering their surface geometries through actuation mechanisms [22–29]. By adjusting their configurations, these systems can adapt to and interact more effectively with various objects. One approach employs grids of individually actuated parallel robots or linear actuators to create distributed manipulation surfaces [24, 30–32]. Another utilizes origami-inspired structures integrated into robotic gripper surfaces to modulate contact friction [33]. To enhance the capabilities of reconfigurable surfaces, modular designs incorporating soft actuators powered by vacuum [34] or origami-inspired actuators [35] have been explored. An alternative approach to address complex manipulation tasks involves integrating nonprehensile manipulation strategies that impose unilateral constraints on the object [36] and manipulating it with proper motion commands mainly based on machine learning principles [37]. A similar methodology includes two serial manipulators to perform complex tasks such as stir-frying which requires a sequence of synchronized and rapid movements [38]. Hu et al. used pneumatic morphological transformation to adjust wettability and manipulate droplets on a surface undergoing deformation [39]. Surface-based manipulation techniques have also been applied at smaller scales, specifically in the reconfigurable braille displays. These displays use dielectric elastomers [40], electromagnetism [41], or shape-memory alloys [42]. Furthermore, reconfigurable surfaces find applications in shape-changing displays designed for human interaction [23, 25, 26, 29].

Despite these advancements, the practical application of reconfigurable surfaces in complex manipulation tasks remains limited. While the potential has been demonstrated in manipulating objects with simple geometries [43–45], challenges such as

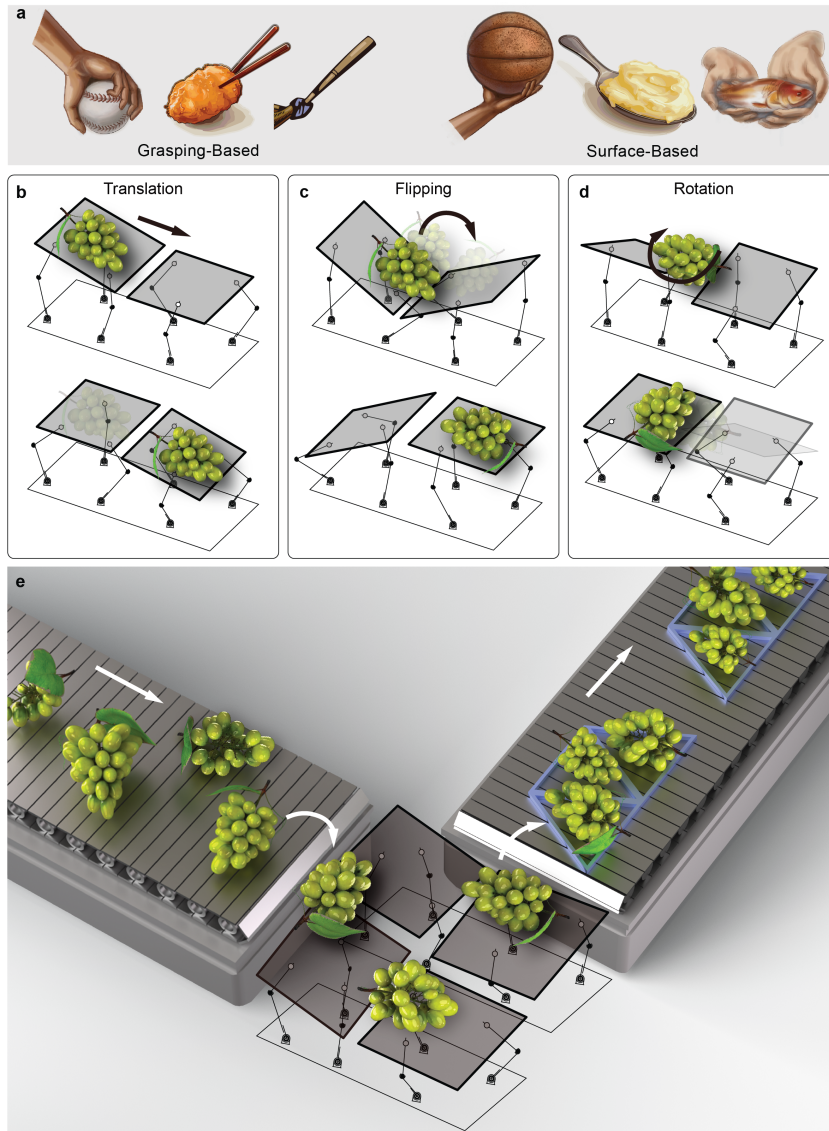


Fig. 1 Surface-based manipulation. (a) In object manipulation contexts, grasping-based interactions such as using chopsticks or hand-grabbing a baseball form our intuition. However, surface-based manipulation plays an equally vital role. For instance, mashed potatoes are typically consumed with a spoon, a surface tool. Similarly, basketballs are often held or supported with palms. Moreover, using hands as a surface support from below makes it easier to hold a wet, slippery fish. For objects with non-conforming shapes or slippery surfaces, utilizing a nonprehensile, surface-based manipulation emerges as an intuitive choice. Building upon this, we present a novel approach to object manipulation using surfaces. This is achieved through the integration of three main motion principles: (b) translation, (c) flipping, and (d) rotation. (e) An example is in food packaging automation, where it addresses the challenge of handling items with varied shapes without causing damage. Surface-based manipulation enables tasks like rotating or positioning grape bunches for packaging and inspection.

limited workspace and slow deformation speeds pose an obstacle for broader scenarios. Additionally, the necessity for continuous surface deformation reduces force output and limits their utility in manipulation contexts. These strategies frequently require the coordinated operation of many modules to manipulate a single object, complicating scalability to larger module sizes and quantities. Consequently, current applications lack dexterous strategies for handling non-rigid or irregularly shaped items and are often confined to specific hardware platforms. These limitations emphasize the need for novel design and actuation methodologies. Exploring innovative approaches to reconfigurable surfaces could significantly advance robotic manipulation, expanding robots' capabilities in handling a diverse range of objects.

Current nonprehensile manipulation methods on reconfigurable surfaces, which utilize individually actuated units, rely heavily on the kinematics of the modules and the sizes of the objects being manipulated. Together, these factors determine the types of nonprehensile motion primitives that can be utilized. Consequently, developing a comprehensive framework to analyze and compare these platforms is crucial for optimizing their design and manipulation strategies. Using information obtained from published literature on several platforms [24, 31, 32, 34, 46–50], we developed a scaling model for surface-based manipulation that results in the mapping of mobility and manipulability of these platforms. Finding the optimal setup for surface-based manipulation involves determining the exact number of DoF needed for each module and how many modules are necessary for different manipulation tasks. Table 1 lists various surface-based object manipulation examples and summarizes their capabilities in terms of repositioning and reorienting objects placed on them. We standardize the module dimensions across the platforms to facilitate comparative analysis, study the relationship between the working modules and manipulability, and highlight their capability in accommodating objects of diverse sizes. The minimum manipulation workspace, MW_{min} , indicates the smallest area where both the functions of the reconfigurable surface and the manipulation strategies are effectively employed. Then, we calculate the minimum mobility requirement, MR_{min} , that represents the necessary number of actuators for different types of surface-based manipulation techniques using single unit DoF, DoF_{SU} , and surface size, SS_{SU} :

$$MR_{min} = \frac{DoF_{SU} \times MW_{min}}{SS_{SU}}. \quad (1)$$

Surfaces consisting of multiple units with one DoF_{SU} can form different profiles from a flat surface, such as slopes for rolling objects or ridges for flipping them, and they enable manipulation of objects larger than SS_{SU} [24, 32, 34, 46]. In these examples, the MR_{min} and consequently the actuator number typically remain relatively high, up to 900, mainly due to the necessary motion primitives and the properties of the manipulated objects [24, 32, 34, 46]. Increasing the DoF_{SU} enables the utilization of additional motion primitives with fewer units. For instance, an example system comprises three DoF_{SU} arranged in an 8×8 configuration [30, 31]. These units, having finger-like end effectors, manipulate objects through coordinated movements such as sliding in addition to rolling [30, 31]. Similarly, Deng et al. introduced a pneumatically actuated soft modular surface with four DoF_{SU} capable of translating and rotating objects through small deformations on the surface [49] and complementary trajectory

Table 1 Overview of existing surface-based manipulation strategies.

Platform	Single Unit DoF, DoF_{SU}	Manip. Modes			Single Unit Surface Size, SS_{SU}	Object Size	Minimum Manip. Workspace, MW_{min}	Minimum Mobility Requirement, MR_{min}
		Tra.	Rot.	Flip.				
WaveHandling [46]	1	✓			$d \times d$	$>d \times d$	$2d \times 2d$	4
Soft Surface [34]	1	✓		✓	$d \times d$	$>2d \times 2d$	$3d \times 3d$	9
inFORM [24]	1	✓	✓	✓	$d \times d$	$>2d \times 2d$	$3d \times 3d$	9
ArrayBot [32]	1	✓	✓	✓	$d \times d$	$>2d \times 2d$	$3d \times 3d$	9
Omnia Wheel [47]	3	✓	✓		$d \times d$	$>2d \times 2d$	$3d \times d$	9
Planar Manip. [48]	3	✓	✓		$d \times d$	$<d \times d$	$d \times d$	3
Delta Arrays [31]	3	✓	✓	✓	$d \times d$	$>2d \times 2d$	$3d \times 3d$	27
Soft Table [49]	4	✓	✓		$d \times d$	$>2d \times 2d$	$3d \times 3d$	36
RoDyMan [50]	12	✓	✓		$d \times d$	$<d \times d$	$d \times d$	12
This Work	3	✓	✓	✓	$d \times d$	$<d \times d$	$2d \times d$	6

planning [51]. Although the number of units is lower in examples with higher DoF_{SU} , the MR_{min} remains high due to the increased actuator number requirements. The introduction of dynamic movements such as vibration has also been shown to facilitate both translation and rotation within the plane [48]. Utilizing a similar methodology, surface-based manipulation extends to serial manipulators through the use of flat-surface end effectors. Ruggiero et al. utilized a dual-arm robot with a total of 12 DoF and employed dynamic manipulation techniques such as rolling, tossing, and batting that translate or rotate objects [36]. Analyzing the MR_{min} aspects of the state-of-the-art reveals a trade-off between the number of required modules and the DoF_{SU} . For instance, a higher DoF_{SU} for fewer units to accomplish the same task. However, increasing the DoF_{SU} poses challenges due to hardware limitations, making it more difficult to expand the SS_{SU} by adding more modules. Consequently, we adopt two units with three DoF_{SU} that represent the minimum configuration required to construct a reconfigurable surface capable of performing dexterous manipulation tasks. This surface consists of individual elements arranged in flat configuration that is able to form three-dimensional configurations and provide synchronized movements upon actuation. The three DoF_{SU} , along with the utilization of the interaction between the two modules, enable a range of dynamic manipulation techniques. This configuration ensures the lowest MR_{min} for surface-based manipulation platforms that can perform object translation, rotation, and flipping (see Fig. 1b-d). The system exhibits scalability in terms of module size, module number, and the size of the object being manipulated. Depending on the specific requirements of the objects, the proposed strategies can be adopted to accommodate different module sizes. Furthermore, increasing the number of modules allows for the application of these strategies to multiple objects simultaneously.

We propose manipulation strategies based on reconfigurable modular surfaces to perform fundamental manipulation tasks such as translating, rotating, and flipping objects of various forms, including non-rigid and irregularly shaped items. We demonstrate these strategies using two identical modular and foldable robots placed side by side to form a reconfigurable surface operating through a decoupled actuation procedure. Each robot is designed, manufactured, and assembled using an origami-based

approach combined with the Canfield joint principle [35, 52–55] and has three DoF. The hierarchical closed-loop control architecture overcomes kinematic constraints and adapts to different robotic platforms, which addresses hardware adaptability issues. By eliminating the need for grasping and continuous surface deformation, our method enables the manipulation of objects with diverse shapes and forms. Quantitative closed-loop experiments validate the overall performance of our system and demonstrate that our approach achieves more dexterous tasks with fewer degrees of freedom compared to other surface-based methods. This work also shows the potential of combining different manipulation strategies to alter the shape of flexible and deformable objects, overcoming existing limitations and expanding the capabilities of robotic manipulation systems. Our approach offers a new perspective for applications such as food packaging (see Fig. 1e) involving reconfigurable surfaces, where automation faces the challenge of handling items with varied and unpredictable shapes without causing damage.

2 Results

The surface-based manipulation in this work involves three strategies: translation, rotation, and flipping (see Fig. 2). To demonstrate the generalizability of surface-based manipulation, we first conducted open-loop teleoperated experiments on a variety of objects and substances of different shapes, sizes, and mechanical properties, including packaged cookies, cakes, a cotton-stuffed toy fish, a roll of tape, and a bag of popcorn (Fig. 3 and Movie S1). We achieved consistent and successful manipulation as our surface-based approach inherently avoids the complexities of grasping, it can accommodate diverse shapes while minimizing stress on the objects.

Building upon the initial demonstrations, we conducted a series of quantitative, vision-based, closed-loop experiments with two modules to evaluate the proposed strategies. Incorporating perception capabilities, our closed-loop control algorithms enhanced the precision and robustness of these manipulation tasks. First, we validated the translation task, an essential foundation for several subsequent tasks, by repositioning objects to desired locations on the entire surface (Fig. 4 and Movie S2). Next, we combined translation and flipping strategies to fully flip planar objects, effectively swapping their top and bottom surfaces, as shown in Fig. 5a-b and Movie S3. The third experiment involves changing the orientation of the object in the middle of two surfaces (Fig. 5c-d and Movie S4). Beyond these pick-and-place tasks, we demonstrated more dexterous manipulations by reshaping a deformable object by folding it to alter its length, as shown in Fig. 6 and Movie S5.

2.1 Translation of Soft and Randomly Shaped Objects

Translating an object is essential in robotic manipulation for repositioning objects and preparing them for subsequent operations. In this work, the first translation analysis involved a randomly shaped object, Play-Doh putty, specifically chosen for its soft and deformable properties. These characteristics present a challenge for conventional grippers, making the object an ideal candidate for testing the capability of our strategy in handling complex material properties.

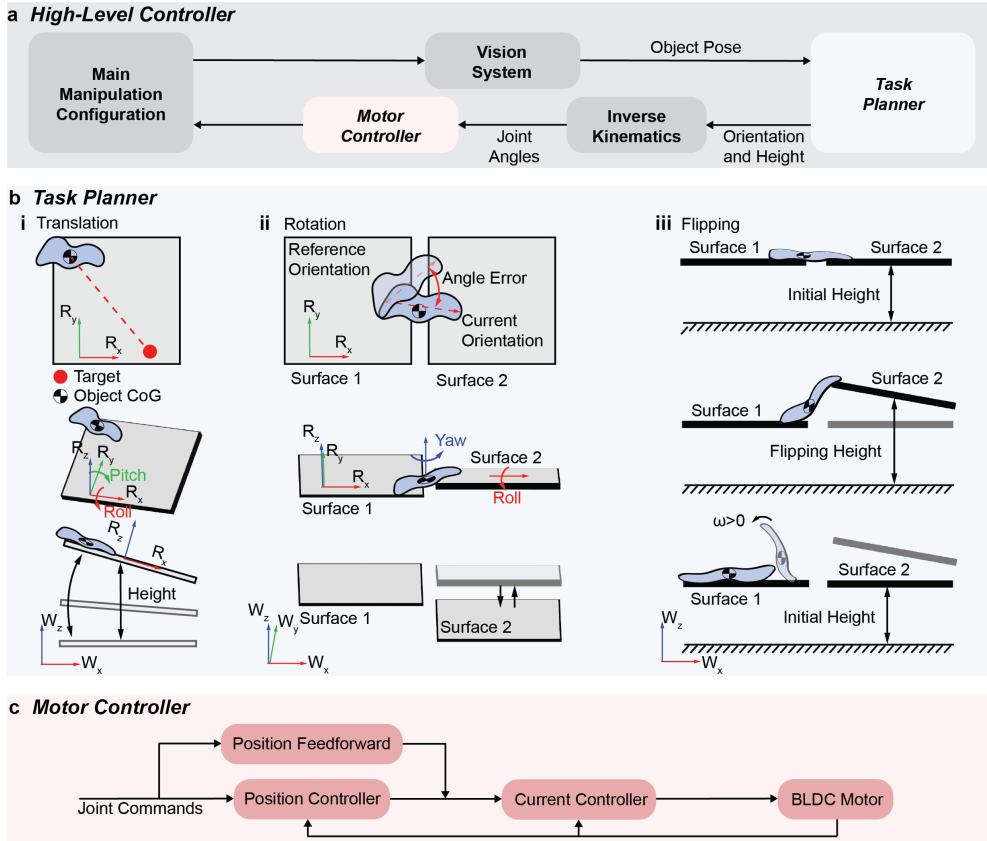


Fig. 2 Control schematic for surface-based object manipulation. (a) High-level controller involves five main components. Main manipulation configuration includes two modules side by side. The vision system captures the object's position and orientation and provides real-time feedback to task planner. (b) The task planner, a state machine, defines surface orientations and height and then these are converted into joint reference positions via inverse kinematics. It transitions among three tasks: (i) translation, (ii) flipping, (iii) and rotation. Translation adjusts the surface's roll and pitch to move the object, followed by height oscillations. Rotation has two phases: Phase 1 adjusts Surface 2's roll, and Phase 2 raises and lowers it to repeat Phase 1 until the desired angle is achieved. Flipping occurs through the rapid elevation of Surface 2. (c) The low-level controller uses BLDC motors with a servo position controller to track joint angle commands with real-time feedback.

The objective is to move the soft object across the surface, starting from varying initial locations but converging to a consistent reference position by closed-loop control (see Fig. 3b and Fig. 4). In Fig. 4a, we illustrate three sequential manipulation paths, each initiated from a distinct starting position. Upon reaching the target position and achieving a steady state, we manually repositioned the object to a new starting point. Despite the different starting points, each route consistently concluded at the same predetermined location in the top-left quadrant of the surface. As shown Fig. 4b, the object consistently returns to its target after manual displacements, guided by the control strategy and continuous adjustments in surface orientation and height. During

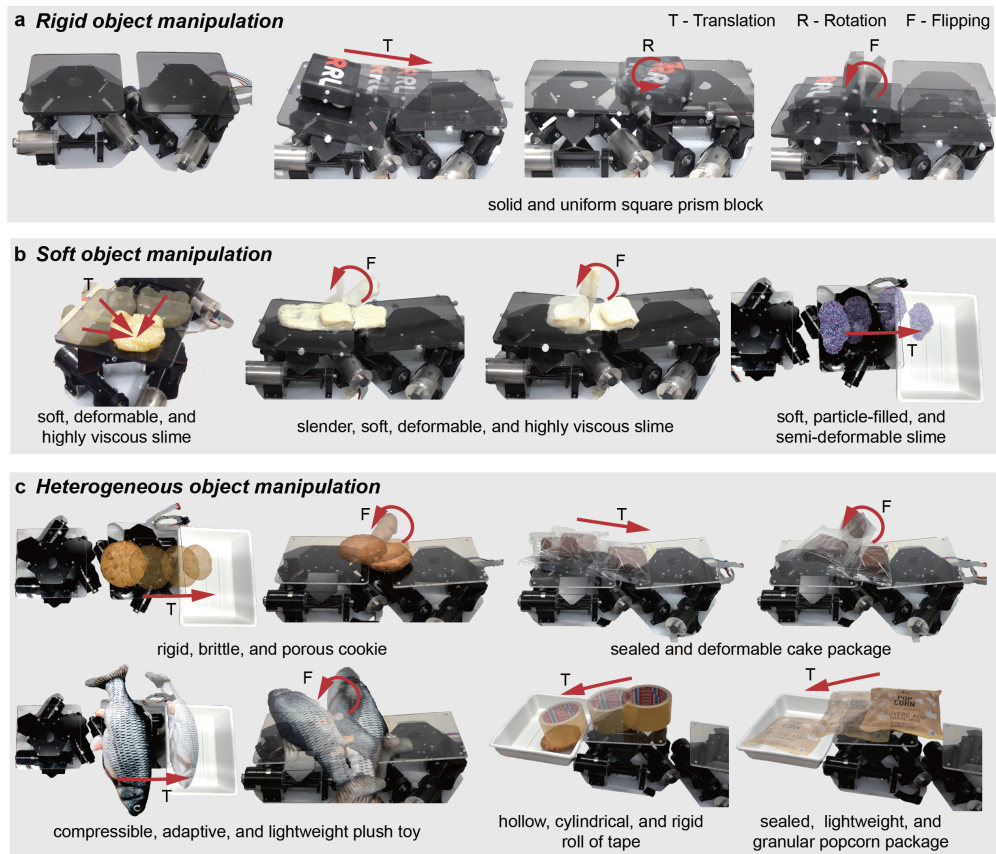


Fig. 3 Surface-based manipulation of various types of objects. Rigid objects and the first two white soft objects are manipulated using closed-loop control, while the remaining manipulations use open-loop teleoperation to transition between different states, demonstrating the strategy’s versatility across diverse object types. (a) Rigid object transfer, flipping, and reorientation. (b) Manipulation of soft and deformable objects: adjusting the position or shape of deformable materials in various forms. (c) Manipulation of different objects, from top left to bottom right: a cookie, a cake in a transparent package, a cotton-stuffed toy fish, a roll of tape, and a bag of unevenly distributed popcorn.

Translation 1, positional changes along the X-axis induced significant variations in surface’s pitch. Before Translation 2, placing the object diagonally opposite the target influenced both the surface’s pitch and roll, with roll adjustments more pronounced due to asymmetries in the workspace (see Fig. S1 and Fig. S2). In Translation 3, the primary deviation along the Y-axis mainly affected surface’s roll values, while minor X-axis changes near the end introduced slight pitch alterations. Additionally, height adjustments in each control cycle caused oscillations that moved the object toward its target.

Across six trials (see Movie S2), the object achieved average velocities of 5.62 cm/s along X-axis and 5.55 cm/s along Y-axis, with steady-state errors of 1.14 cm and 0.87 cm, respectively. Subtle positional discrepancies likely arose from differences in

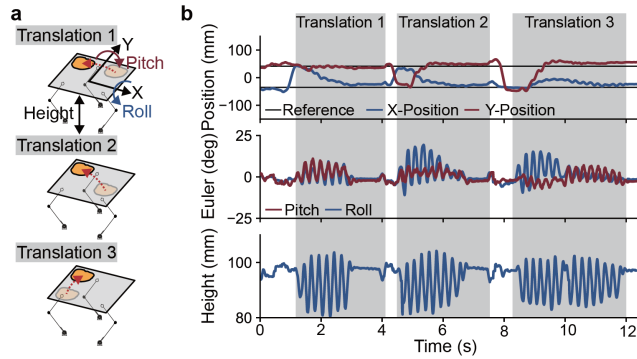


Fig. 4 Translation of soft objects. In this experiment, the efficacy of our translation strategy was assessed using a deformable object positioned at multiple initial locations. (a) Initial setup for three sequential tests with object: Lighter colors indicate initial positions and darker colors show target positions. Objects are manually reset to new initial positions after each translation. (b) The object’s trajectory in the XY-plane and surface adjustments in roll, pitch, and height are controlled by the transfer strategy.

achievable tilt angles (Fig. S2). Overall, these results confirm that our manipulation strategy reliably directs objects to their intended targets, even from various starting points, while minimizing deformation of soft objects.

2.2 Translation and Flipping of Rigid Object

Flipping motions are crucial in both industrial applications such as assembly and food inspection on production lines [56] and domestic robotics for household tasks [57]. Flipping typically requires multiple controllable contact points [58] and necessitates complex manipulators or dual-arm robots working in coordination [59]. It also demands accurate modeling of contact interactions, handling uncertainties, and maintaining grasp stability. Additionally, limitations in the end effector’s workspace and kinematics further complicate the execution of flipping motions. These complexities make traditional manipulation strategies inadequate for efficiently automating flipping tasks. Our approach addresses these issues by removing workspace dependence through nonprehensile dynamic motion enabled by coordinated modular interactions. This strategy executes complex tasks like 180° flipping along a horizontal axis without intricate grasping mechanisms or high DoF.

We tested this approach by first translating an object from a random starting position on Surface 1 to the intersection of two surfaces (see Fig 3a). Knowing the object’s dimensions, we designed the target position so that the object makes contact with Surface 2 while its center of gravity remains on Surface 1. This setup facilitated the flipping maneuver. After the flip, we repositioned the object between the surfaces and repeated these operations to validate both translation and flipping strategies. As shown in Fig. 5a-b and Fig. 3a, the object was initially moved into position, flipped 180° around its Y-axis, and then returned to an intermediate location between the surfaces. Fig. 5b tracks the object’s trajectory, confirming its successful realignment. During the flipping phase, rapid height and orientation adjustments of Surface 2 briefly impacted the object, completing the flip and producing a distinct yaw change around second

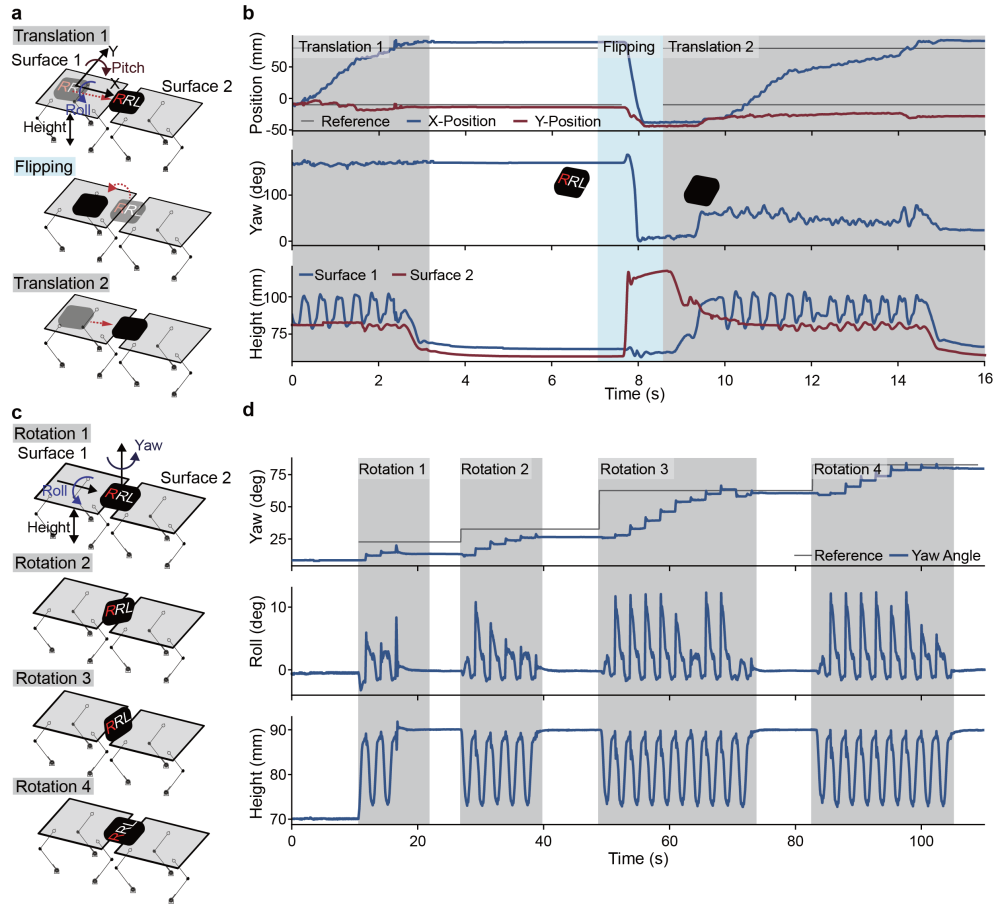


Fig. 5 Validation of translation, flipping, and rotation strategies for rigid objects. (a) In translation and flipping experiments, the object (measuring $8\text{cm} \times 8\text{cm} \times 3\text{cm}$ and weighing 110g) translates from an initial point on Surface 1 to between two surfaces and then flips. After flipping, the object's position shifts towards Surface 1, and it is translated again between two surfaces. (b), the position of the object in the surface frame is depicted over time. A noticeable 180° transition in the object's yaw orientation in the global frame is attributed to the flipping motion. Additionally, changes in the height of Surface 1 and Surface 2 during manipulation are shown. (c) The schematic shows the rotation experiment setup with the object positioned between the two surfaces. The experiment sets four reference angles of 20° , 30° , 60° , and 80° and aims to rotate the object to the target orientation. (d) The reference angle and the object's actual orientation are compared. It also highlights the dynamic adjustments in Surface 2's roll and height during operation.

8. Overall, these results demonstrate that our surface-based manipulation method efficiently handles complex flipping tasks, expanding the capabilities of surface-based manipulation strategies.

2.3 Rotation of Rigid Object

In assembly lines or food production processes, objects often need to be aligned to specific angles before packaging or further handling [60]. To demonstrate the surface-based manipulation approach for reorienting objects, we conducted an experiment to rotate a rigid object within the surfaces around the Z-axis from its initial orientation to various target orientations. Fig. 5c presents a schematic of our experimental setup that utilizes a square prism as the object of manipulation. Building on the success of the transfer strategy validated in the previous experiment, we assumed the object’s initial position to be centered between two surfaces, with its center of gravity resting on one surface, and then adjusted the other surface’s roll and height to achieve a series of target angles. In Fig. 5d, the actual yaw angles of the object and its alignment with the set target angles are shown. A new reference angle is assigned after the object reaches a reference position. Fig. 5d also displays the roll angle and height adjustments of Surface 1. The variation in Surface 1’s roll angle tends to decrease as the discrepancy between the object’s current angle and the reference angle reduces. The maximum surface’s roll angle per cycle, controlled by a low-level PID controller, is capped at 12° . During the experiments, we achieved an average rotational velocity of $1.16^\circ/s$. Following each interaction with the object through roll movement, the surface lowers in altitude and adjusts to an offset angle, preparing for the next interaction cycle. Through this experiment, we successfully validated the feasibility of our rotation strategy and demonstrated a novel, nonprehensile approach to reorientation.

2.4 Shape Manipulation of Deformable Object

Manipulating deformable objects is essential in various fields [61], including manufacturing [62], the food handling [63], healthcare [64], and elderly care [65]. However, automating the handling of deformable objects remains a significant challenge due to the highly nonlinear character of these materials, which makes accurate modeling extremely difficult [21, 66]. Additionally, using grasping-based methods can cause further unpredictable deformations during manipulation [65]. Surface-based manipulation simplifies perception and control requirements because it reduces the complexity associated with modeling contact dynamics and grasp stability. In this experiment, we combined the previously introduced strategies to fold a strip of putty multiple times, relying only on measurements of the object’s length and geometric center, showcasing the endless possibilities of surface-based methods. Extending this strategy to additional or larger modules could potentially enable more complex tasks involving deformable objects, such as folding clothes or kneading dough.

In Fig. 3b and Fig. 6a, we show the process of folding a strip deformable object. In the experiment, we track the length and geometric center of the deformable object strip using a camera and apply a combination of the previously proposed transfer and flipping strategies to achieve the folding of the deformable object. At the initial stage of the experiment, we positioned the object between two surfaces, upon which we implemented our flipping strategy. However, as the object being manipulated is a soft continuum this time, only a part folds rather than undergoing a complete flip. The folding alters the object’s length, and since we are tracking its geometric center,

its position coordinates also change instantaneously. The position coordinates of the tracked object, as shown in Fig. 6b, indicate that the first fold occurs at second 1. The variations in object length are displayed in Fig. 6b. Subsequently, we implemented the translation strategy to position the object between the two surfaces for the next folding phase, as shown during the transfer stage in Fig. 6b. Given our knowledge of the object’s length and the aim to fold approximately one-third of it in each attempt, we were able to determine the target reference positions based on the anticipated length of the fold. This approach allowed for precise control of the folding process. We executed the second folding motion once the object reached the reference position. Finally, through the integration of these operations, we successfully transformed a deformable object strip into a rolled-up configuration and changed its length. This demonstrates the versatility of surface-based manipulation and their potential applications across various fields.

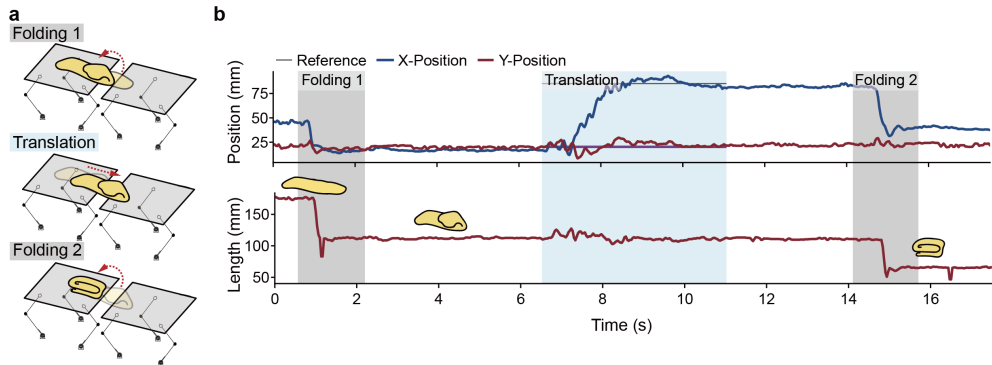


Fig. 6 Shape manipulation of free-form objects. (a) Method for folding a long strip of a deformable object. The process starts with a flip for Folding 1, followed by a translation step to adjust the object for contact with both surfaces and then followed by Folding 2. (b) The object’s XY-position and length changes throughout the experiment, with noticeable shifts at second 1 and second 15. These shifts occur because folding alters the object’s geometry, which affects both its geometric center and the camera’s tracking center.

3 Discussion

In this work, we presented a method to overcome the challenge of manipulating soft and deformable objects utilizing modular robotic surfaces and successfully demonstrated three fundamental operations: translation, rotating, and flipping objects on the surface. Unlike traditional grasping methods that require selecting specific grasp points and struggle with large, low-friction, or deformable objects, our surface-based approach inherently extends to objects of different shapes, sizes, and stiffness levels. The hierarchical control structure enables the proposed strategies to be adapted to other hardware setups by using a simple plane as the end-effector and ensuring the hardware has roll, pitch, and height degrees of freedom. For instance, two conventional

six-degree-of-freedom robotic arms equipped with plane end-effectors can apply the strategies presented in this study.

Our work offers a new perspective on manipulation, particularly for handling deformable, soft, and fragile objects. This has potential applications in industrial production and the food industry, where packaging and handling of soft, deformable objects like chicken or fish, which are typically slippery and easily damaged, present significant challenges when using traditional gripper-based methods. Using vision-based closed-loop feedback, we achieved robust control by tracking the geometric center position and orientation of objects with known shapes and sizes. However, our current approach faces limitations in more dynamic environments, especially when the shape of the objects is unknown. For example, flipping and rotating may not be effective if the object’s shape is not accurately perceived. Future work could integrate more sophisticated perception algorithms to understand object shapes better and employ learning-based control algorithms to adapt to different objects and more dynamic environments.

4 Methods

This section describes the system’s design and the perception and control methods for manipulating non-spherical objects on reconfigurable surfaces. We employ an origami-inspired foldable three-DoF parallel mechanism to achieve compactness while providing flexible joint actuation and a large workspace. For closed-loop control, we developed vision-based method to track the object’s pose in real time. Additionally, we proposed a hierarchical control strategy that outputs commands directly at the end-effector pose level rather than at the joint level for coordination among multiple modules, which makes the control strategy applicable to varying numbers of modules and diverse geometric configurations.

4.1 Surface-Based Integrated Design

The reconfigurable surface implemented in this project comprises two identical robotic modules. Each module has five main components (see Fig. S1(a)). The surface platform is manufactured from an acrylic sheet, serving as the interface for contacting and manipulating objects via reconfigurability. The origami legs consist of a polyimide layer sandwiched between two FR4 layers, adhered together using two adhesive layers activated through a heat press application. The origami design derives from the fundamental waterbomb origami fold that can enable motion across three DoF, similar to the structures and their functionalities in the previous works [35, 53–55, 67]. The legs facilitate the system’s reconfigurability, with each leg actuated by direct-driven BLDC motors (maxon EC-i 40) linked with 3D-printed PLA connectors. Finally, the base platform fabricated from an acrylic sheet secures the module onto the surface where the modules are fixed. Each motor, allocated to actuate the robotic modules, operates with a 36V nominal voltage and can generate a nominal torque of up to $207mN.m$. The STSPIN32F0A module (by STMicroelectronics) performs low-level control of the motors and manages the required current flow from the power supply.

A main controller unit (Teensy MicroMod by PJRC and SparkFun) functions to handle high-level control operations and coordinates communication between these two boards. This communication utilizes the MODBUS RS-485 protocol and the Teensy controller's TTL output. MAX485 module converts the main controller's TTL output to the MODBUS RS-485 protocol, creating a coherent and reliable communication channel between the low-level actuation control and high-level functions.

4.2 Integrated Perception Systems for Real-Time Object States Tracking on Surfaces

In order to obtain accurate position and orientation data for both the object positioned on the reconfigurable surface and each individual module's surface, we employed a perception system based on computer vision. For objects characterized as nearly-rigid, we utilized a motion capture setup, equipped with six high-field-of-view and high-precision cameras (Vicon Vero). These objects carried deliberately placed markers to perform accurate tracking. The data obtained from the motion capture system was then transferred to the closed-loop control setup through an I2C communication protocol that was set to operate at a frequency of $100Hz$. We adopted an alternative approach for the objects having deformable materials and non-rigid behavior where marker attachment is not possible. A camera-based custom image processing setup was established, employing a Logitech C270 webcam and OpenCV. This setup was utilized to detect the object's geometrical center and its boundaries. These methods enabled us to obtain the position feedback for manipulating both deformable and non-deformable objects on the reconfigurable surface.

4.3 Control System Overview and Implementation

The overall control of the developed system includes five main components (Fig. 2). Manipulation strategy transitions are managed by predefined task objectives. This system employs a state machine that dynamically alters between three modes: translation, rotation, and flipping. The position and the orientation of the object are obtained by the real-time sensor data from the vision system, guiding the dynamic generation of the surfaces' roll, pitch, and height references in accordance with the appropriate manipulation strategy. Using the inverse kinematics algorithm explained in Method S1, the desired joint angles are computed. These reference values are then input into a PID-based servo motor controller, ensuring precise trajectory tracking of the joint commands. In the control scheme for the BLDC motor, as illustrated in Fig. 2c, a cascade control structure is implemented, comprising both a feedforward component and a current loop within the position loop.

4.4 High-Level Controller for Three Different Surface-Based Manipulation Strategies: Translation, Rotation, Flipping

Translation

Surface-based manipulation enables moving an object from any initial position to a specified target. Our translation strategy focuses on objects that fit entirely on a

single surface. As shown in Fig. 2, given the object’s current center of gravity (CoG) position, the goal is to move its centroid to the target. Here, X_{error} and Y_{error} are the positional errors along the local X- and Y-axes of the surface.

We define the surface orientation with XYZ-Euler angles and set $yaw = 0$ due to the Canfield structure’s directional constraint. Algorithm 1 outlines the complete procedure. Each control cycle computes pitch and roll references based on X_{error} and Y_{error} , with a PID controller determining the exact angles (Fig. 2b and Eq. 2):

Algorithm 1 Translation Strategy

```

1: procedure TRANSLATION( $X_{ref}, Y_{ref}, X_{cur}, Y_{cur}, \epsilon$ )
2:   # Line 3-4: compute the position error between the target and the object’s
   current position.
3:    $X_{error} = X_{ref} - X_{pos}$ 
4:    $Y_{error} = Y_{ref} - Y_{pos}$ 
5:   while  $|X_{error}| + |Y_{error}| \geq \epsilon$  do
6:     # Line 7-10: if the positional error exceeds  $\epsilon$ , calculate the reference pose
     for the surface.
7:      $\theta_{surface\_roll} = PID(Y_{error})$  ▷ Equation 2
8:      $\theta_{surface\_pitch} = PID(X_{error})$  ▷ Equation 2
9:      $H = A \sin(\omega t) + H_{init}$  ▷ Equation 3
10:     $Surface \leftarrow [\theta_{Surface1\_roll}, \theta_{surface\_pitch}, H]$ 
11:  end while
12: end procedure

```

$$\begin{aligned}
Ref_{roll} &= K_P Y_{error}(t) + K_i \int_0^t Y_{error}(\tau) d\tau + K_d \frac{d}{dt} Y_{error}, \\
Ref_{pitch} &= K_P X_{error}(t) + K_i \int_0^t X_{error}(\tau) d\tau + K_d \frac{d}{dt} X_{error}.
\end{aligned} \tag{2}$$

In low-friction scenarios, where the friction coefficient μ is smaller than $\tan(\psi)$ (the tangent of the surface’s normal vector polar angle ψ), the control approach resembles a classic ball balancing table. Here, adjusting the surface’s inclination smoothly guides the object to its target. Under higher friction, inclination alone may not suffice. To overcome this, we modulate the surface’s height as well as its orientation (Fig. 2b), introducing vertical oscillations that reduce frictional resistance and apply periodic impulses to move the object. We define:

$$H = A \sin(\omega t) + H_{init}, \tag{3}$$

where t is the elapsed time and ω is the oscillation frequency, adjustable to suit different objects. The elevation of the surface also affects its maximum achievable tilt angle (see Fig. S2). To maintain a large range of motion, here the vertical displacement amplitude spans from 8 cm to 10 cm.

Using Euler angles, the rotation matrix of the top surface can be calculated in Equation 4, where ϕ is the reference roll angle, and θ is the reference pitch angle:

$$C_{WR} = \begin{bmatrix} \cos(\theta) & 0 & \sin(\theta) \\ \sin(\phi)\sin(\theta) & \cos(\phi) & -\cos(\theta)\sin(\phi) \\ -\cos(\phi)\sin(\theta) & \sin(\phi) & \cos(\phi)\cos(\theta) \end{bmatrix}. \quad (4)$$

Neglecting vertical translation, the top surface's normal vector is:

$$N_{O_R} = C_{WR} * [0, 0, 1]^T = [\sin(\theta), -\cos(\theta)\sin(\phi), \cos(\phi)\cos(\theta)]^T. \quad (5)$$

From N_{O_R} , we derive the polar and azimuthal angles of the surface:

$$\begin{aligned} \delta &= \arctan\left(\frac{N_{O_R}(y)}{N_{O_R}(x)}\right) = \arctan\left(\frac{-\cos(\theta)\sin(\phi)}{\sin(\theta)}\right), \\ \psi &= \arccos(N_{O_R}(z)) = \arccos(\cos(\phi)\cos(\theta)). \end{aligned} \quad (6)$$

Once we determine the required orientation and height parameters (δ, ψ, H) for the Canfield mechanism's end-effector, we apply inverse kinematics (Method S1, Chapter 4.4) to compute the corresponding joint angles.

Rotation

We achieve surface-based object rotation by repeatedly establishing and breaking contact between the object and multiple surfaces. As the object interacts with these surfaces, their differing force directions enable complex rotational maneuvers (see Fig. 2b). We define the object's current yaw angle as θ_{yaw} and the target angle as θ_{ref} .

Building on the XYZ-Euler angle coordinate, we modulate Surface 2's roll angle to induce torque on the object (Fig. 2b), as determined by a PID controller (Eq. 7):

$$\theta_{surface2.roll} = K_P * \theta_{error}(t) + K_i \int_0^t \theta_{error}(\tau) d\tau + K_d \frac{d}{dt} \theta_{error}. \quad (7)$$

Algorithm 2 details the rotation procedure. Each cycle adjusts surface angles to exert torque, then returns them to a neutral state, ensuring fresh contact points for subsequent cycles. During rotation, we adjust the pitch angle of Surface 1 to incline toward the center, against object displacement along the X-axis. Additionally, the roll of Surface 1 is also adjusted by a fixed angle θ_γ in correspondence with the object's rotation direction, further facilitating the object's rotation. In cases where the surface reaches its maximum roll angle before achieving the target object orientation, we realign the surfaces horizontally and then raise Surface 2 back to its initial height, providing a renewed contact interface (Algorithm 2 line 19-20). If the object still does not reach the desired angle, the algorithm repeats these steps (Algorithm 2 line 6-21) until convergence.

Flipping

Flipping an object by 180° requires surface delivering substantial impulses within a brief timescale. As shown in Fig. 2b, our approach begins with the object positioned

Algorithm 2 Rotation Strategy

```
1: procedure ROTATION( $\theta_{ref}, \theta_{yaw}, \epsilon$ )
2:   # Line 3-4: initialize the surface.
3:    $Surface_1 \leftarrow [0, 0, H_{init}]$ 
4:    $Surface_2 \leftarrow [0, 0, H_{init}]$ 
5:   # Line 6-21: repeat when the angular error between the object's current angle
and target angle exceeds  $\epsilon$ . This constitutes one cycle.
6:   while  $|\theta_{ref} - \theta_{yaw}| \geq \epsilon$  do
7:      $\theta_{surface2.roll} = PID(\theta_{ref} - \theta_{yaw})$  ▷ Equation 7
8:     if  $\theta_{surface2.roll} \geq 0$  then
9:        $\theta_{Surface1.roll} = -\theta_\gamma$ 
10:    else
11:       $\theta_{Surface1.roll} = \theta_\gamma$ 
12:    end if
13:    # rotate the surface to the reference pose to induce the object's rotation.
14:     $Surface_1 \leftarrow [\theta_{Surface1.roll}, -\theta_\beta, H_{init}]$ 
15:     $Surface_2 \leftarrow [\theta_{Surface2.roll}, -\theta_\beta, H_{init}]$ 
16:    delay 500ms
17:    # reset the surface after one cycle to establish new contact points in next
cycle.
18:     $Surface_1 \leftarrow [0, 0, H_{init}]$ 
19:     $Surface_2 \leftarrow [0, \theta_\beta, H_{low}]$ 
20:     $Surface_2 \leftarrow [0, \theta_\beta, H_{init}]$ 
21:  end while
22:  # Line 23-24: reset the surface once the object reaches the reference angle to
prepare for the next task.
23:   $Surface_1 \leftarrow [0, 0, H_{init}]$ 
24:   $Surface_2 \leftarrow [0, 0, H_{init}]$ 
25: end procedure
```

in contact with two surfaces, with its CoG falling into Surface 1. To initiate a flipping around a specific contact point, Surface 2 undergoes a rapid elevation, exerting a continuous force onto the object's one edge. To enhance this rotational trajectory, Surface 2's initial ascent deviates from a horizontal orientation by adopting a fixed angular tilt relative to the Y-axis as detailed in line 9 of Algorithm 3.

As Surface 2 pushes upward, the object's angular velocity increases. Eventually, Surface 2 reaches its maximum elevation and loses contact, leaving the object to continue rotating under gravity alone. For a successful flip, the object's angular velocity must remain positive when the line connecting its CoG and the contact point becomes perpendicular to the surface, allowing gravity to complete the rotation.

Let ω_{t1} be the angular velocity of the object when it separates from Surface 2. The kinetic energy at this point must be equal to or surpass its gravitational potential energy for the flipping action to succeed. Mathematically, this is expressed as follows:

Algorithm 3 Flipping Strategy

```
1: procedure FLIPPING
2:   # Line 3-5: based on the object's size, transport it from the initial position to
   a flipping position between the two surfaces.
3:   if  $\|(X_{ref}, Y_{ref}) - (x, y)\| > \epsilon$  then
4:      $Surface_1 \leftarrow transfer(X_{ref}, Y_{ref})$  ▷ Algorithm 1
5:      $Surface_2 \leftarrow [0, -\theta_\beta, H_{init} - 1]$ 
6:   else
7:     # Line 8-9: Lower the surface to initialize the flipping task.
8:      $Surface_1 \leftarrow [0, 0, H_{low}]$ 
9:      $Surface_2 \leftarrow [0, \theta_\beta, H_{low}]$ 
10:     $delay\ 5000ms$ 
11:     $Surface_1 \leftarrow [0, 0, H_{low}]$ 
12:    # Quickly raise Surface 2 to generate an impact, flipping the object.
13:     $Surface_2 \leftarrow [0, 0, H_{high}]$  in 100ms
14:     $delay\ 1000ms$ 
15:    # Line 16-17: after flipping, reset the surface to prepare for the next task.
16:     $Surface_1 \leftarrow [0, 0, H_{init}]$ 
17:     $Surface_2 \leftarrow [0, 0, H_{init}]$ 
18:  end if
19: end procedure
```

$$0 - \frac{1}{2}J\omega_{t1}^2 \geq \frac{L}{2}mg(\sin(\theta) - 1), \quad (8)$$
$$\omega_{t1_min} = \sqrt{\frac{mgL(1 - \sin(\theta))}{J}}.$$

Where θ is the angle between the target object and the horizontal when Surface 2 detaches, J represents the target object's rotational inertia on this axis, and L is the object's cross-sectional length.

The main strategy is centered on optimizing the linear velocity of Surface 2. Adjusting Surface 2 to reach this critical velocity level can provide the object with enough momentum to overcome gravitational forces:

$$V_{min_vel_required} = L * \omega_{t1_min}. \quad (9)$$

Another approach is to maximize Surface 2's acceleration, pushing it to the highest possible speed. This strategy delivers maximum momentum to the object, reducing uncertainties and increasing the likelihood of a successful flip.

Declarations

Acknowledgements

The authors thank Alexander Schüßler of Reconfigurable Robotics Lab, EPFL for his contributions to using computer vision to identify the position of deformable objects.

Funding

This research has received funding from the European Union’s Horizon Europe research and innovation programme under grant agreement no: 101069536 (MOZART project).

Author contribution

- Conceptualization ZW, SD, FZ, and JP
- Funding acquisition JP
- Investigation ZW, SD
- Methodology ZW, SD, and JP
- Software ZW and SD
- Supervision JP
- Visualization ZW, SD, and FZ
- Writing - original draft ZW and SD
- Writing - review & editing ZW, SD, FZ, and JP

References

- [1] Pfeifer, R., Lungarella, M., Iida, F.: Self-organization, embodiment, and biologically inspired robotics. *Science* **318**(5853), 1088–1093 (2007) <https://doi.org/10.1126/science.1145803>
<https://www.science.org/doi/pdf/10.1126/science.1145803>
- [2] Sun, J., Lerner, E., Tighe, B., Middlemist, C., Zhao, J.: Embedded shape morphing for morphologically adaptive robots. *Nature Communications* **14**(1), 6023 (2023)
- [3] Baines, R., Fish, F., Bongard, J., Kramer-Bottiglio, R.: Robots that evolve on demand. *Nature Reviews Materials*, 1–14 (2024)
- [4] Shah, D.S., Powers, J.P., Tilton, L.G., Kriegman, S., Bongard, J., Kramer-Bottiglio, R.: A soft robot that adapts to environments through shape change. *Nature Machine Intelligence* **3**(1), 51–59 (2021)
- [5] Baines, R., Patiballa, S.K., Booth, J., Ramirez, L., Sipple, T., Garcia, A., Fish, F., Kramer-Bottiglio, R.: Multi-environment robotic transitions through adaptive morphogenesis. *Nature* **610**(7931), 283–289 (2022)

- [6] Gupta, A., Savarese, S., Ganguli, S., Fei-Fei, L.: Embodied intelligence via learning and evolution. *Nature communications* **12**(1), 5721 (2021)
- [7] Pouydebat, E., Boulinguez-Ambroise, G., Manzano, A., Abdala, V., Sustaita, D.: Convergent evolution of manual and pedal grasping capabilities in tetrapods. In: *Convergent Evolution: Animal Form and Function*, pp. 323–389. Springer, Cham (2023)
- [8] Langowski, J.K.A., Sharma, P., Shoushtari, A.L.: In the soft grip of nature. *Science Robotics* **5**(49), 9120 (2020) <https://doi.org/10.1126/scirobotics.abd9120>
<https://www.science.org/doi/pdf/10.1126/scirobotics.abd9120>
- [9] Katzschmann, R.K., Marchese, A.D., Rus, D.: Autonomous object manipulation using a soft planar grasping manipulator. *Soft Robotics* **2**(4), 155–164 (2015) <https://doi.org/10.1089/soro.2015.0013>
- [10] Hao, Y., Wang, Z., Zhou, Y., Zhou, W., Cai, T., Zhang, J., Sun, F.: A soft enveloping gripper with enhanced grasping ability via morphological adaptability. *Advanced Intelligent Systems* **5**(6), 2200456 (2023)
- [11] Howard, G.D., Brett, J., O’Connor, J., Letchford, J., Delaney, G.W.: One-shot 3d-printed multimaterial soft robotic jamming grippers. *Soft Robotics* **9**(3), 497–508 (2022). PMID: 34107745
- [12] Spiers, A.J., Liarakapis, M.V., Calli, B., Dollar, A.M.: Single-grasp object classification and feature extraction with simple robot hands and tactile sensors. *IEEE Transactions on Haptics* **9**(2), 207–220 (2016) <https://doi.org/10.1109/TOH.2016.2521378>
- [13] Liu, H., Zhao, L., Siciliano, B., Ficuciello, F.: Modeling, optimization, and experimentation of the paragripper for in-hand manipulation without parasitic rotation. *IEEE Robotics and Automation Letters* **5**(2), 3011–3018 (2020) <https://doi.org/10.1109/LRA.2020.2974419>
- [14] Khadivar, F., Billard, A.: Adaptive fingers coordination for robust grasp and in-hand manipulation under disturbances and unknown dynamics. *IEEE Transactions on Robotics* **39**(5), 3350–3367 (2023) <https://doi.org/10.1109/TRO.2023.3280028>
- [15] Firouzeh, A., Paik, J.: Grasp mode and compliance control of an underactuated origami gripper using adjustable stiffness joints. *IEEE/ASME Transactions on Mechatronics* **22**(5), 2165–2173 (2017) <https://doi.org/10.1109/TMECH.2017.2732827>
- [16] Chen, R., Zhang, C., Sun, Y., Yu, T., Shen, X.-M., Yuan, Z.-A., Guo, J.-L.: A paper fortune teller-inspired reconfigurable soft pneumatic gripper. *Smart Materials and Structures* **30**(4), 045002 (2021) <https://doi.org/10.1088/1361-665X/>

- [17] Shintake, J., Rosset, S., Schubert, B., Floreano, D., Shea, H.: Versatile soft grippers with intrinsic electroadhesion based on multifunctional polymer actuators. *Advanced Materials* **28**(2), 231–238 (2016)
- [18] Piskarev, Y., Devincenti, A., Ramachandran, V., Bourban, P.-E., Dickey, M.D., Shintake, J., Floreano, D.: A soft gripper with granular jamming and electroadhesive properties. *Advanced Intelligent Systems* **5**(6), 2200409 (2023) <https://doi.org/10.1002/aisy.202200409>
- [19] Shintake, J., Cacucciolo, V., Floreano, D., Shea, H.: Soft robotic grippers. *Advanced Materials* **30**(29), 1707035 (2018) <https://doi.org/10.1002/adma.201707035> <https://onlinelibrary.wiley.com/doi/pdf/10.1002/adma.201707035>
- [20] Zhang, B., Xie, Y., Zhou, J., Wang, K., Zhang, Z.: State-of-the-art robotic grippers, grasping and control strategies, as well as their applications in agricultural robots: A review. *Computers and Electronics in Agriculture* **177**, 105694 (2020) <https://doi.org/10.1016/j.compag.2020.105694>
- [21] Billard, A., Kragic, D.: Trends and challenges in robot manipulation. *Science* **364**(6446), 8414 (2019)
- [22] Rasmussen, M.K., Pedersen, E.W., Petersen, M.G., Hornbæk, K.: Shape-changing interfaces: a review of the design space and open research questions. In: *Proceedings of the SIGCHI Conference on Human Factors in Computing Systems*, pp. 735–744 (2012)
- [23] Alexander, J., Roudaut, A., Steimle, J., Hornbæk, K., Bruns Alonso, M., Follmer, S., Merritt, T.: Grand challenges in shape-changing interface research. In: *Proceedings of the 2018 CHI Conference on Human Factors in Computing Systems*, pp. 1–14 (2018)
- [24] Follmer, S., Leithinger, D., Olwal, A., Hogge, A., Ishii, H.: inform: dynamic physical affordances and constraints through shape and object actuation. In: *Uist*, vol. 13, pp. 2501–988 (2013). Citeseer
- [25] Grønbaek, J.E., Rasmussen, M.K., Halskov, K., Petersen, M.G.: Kirigamitable: Designing for proxemic transitions with a shape-changing tabletop. In: *Proceedings of the 2020 CHI Conference on Human Factors in Computing Systems*, pp. 1–15 (2020)
- [26] Steed, A., Ofek, E., Sinclair, M., Gonzalez-Franco, M.: A mechatronic shape display based on auxetic materials. *Nature Communications* **12**(1), 4758 (2021)
- [27] Hwang, D., Barron III, E.J., Haque, A.T., Bartlett, M.D.: Shape morphing mechanical metamaterials through reversible plasticity. *Science robotics* **7**(63),

- [28] Tahouni, Y., Qamar, I.P., Mueller, S.: Nurbsforms: A modular shape-changing interface for prototyping curved surfaces. In: Proceedings of the Fourteenth International Conference on Tangible, Embedded, and Embodied Interaction, pp. 403–409 (2020)
- [29] Siu, A.F., Gonzalez, E.J., Yuan, S., Ginsberg, J.B., Follmer, S.: Shapeshift: 2d spatial manipulation and self-actuation of tabletop shape displays for tangible and haptic interaction. In: Proceedings of the 2018 CHI Conference on Human Factors in Computing Systems, pp. 1–13 (2018)
- [30] Thompson, S., Mannam, P., Temel, Z., Kroemer, O.: Towards robust planar translations using delta-manipulator arrays. In: 2021 IEEE International Conference on Robotics and Automation (ICRA), pp. 6563–6569 (2021). <https://doi.org/10.1109/ICRA48506.2021.9561003>
- [31] Patil, S., Tao, T., Hellebrekers, T., Kroemer, O., Temel, F.Z.: Linear delta arrays for compliant dexterous distributed manipulation. In: 2023 IEEE International Conference on Robotics and Automation (ICRA), pp. 10324–10330 (2023)
- [32] Xue, Z., Zhang, H., Cheng, J., He, Z., Ju, Y., Lin, C., Zhang, G., Xu, H.: Arraybot: Reinforcement learning for generalizable distributed manipulation through touch. In: 2024 IEEE International Conference on Robotics and Automation (ICRA), pp. 16744–16751 (2024). <https://doi.org/10.1109/ICRA57147.2024.10610350>
- [33] Lu, Q., Clark, A.B., Shen, M., Rojas, N.: An origami-inspired variable friction surface for increasing the dexterity of robotic grippers. *IEEE Robotics and Automation Letters* **5**(2), 2538–2545 (2020)
- [34] Robertson, M.A., Murakami, M., Felt, W., Paik, J.: A compact modular soft surface with reconfigurable shape and stiffness. *IEEE/ASME Transactions on Mechatronics* **24**(1), 16–24 (2018)
- [35] Salerno, M., Paik, J., Mintchev, S.: Ori-Pixel, a multi-DoFs origami pixel for modular reconfigurable surfaces. *IEEE Robotics and Automation Letters* **5**(4), 6988–6995 (2020)
- [36] Ruggiero, F., Lippiello, V., Siciliano, B.: Nonprehensile dynamic manipulation: A survey. *IEEE Robotics and Automation Letters* **3**(3), 1711–1718 (2018)
- [37] Sun, X., Li, J., Kovalenko, A.V., Feng, W., Ou, Y.: Integrating reinforcement learning and learning from demonstrations to learn nonprehensile manipulation. *IEEE Transactions on Automation Science and Engineering* **20**(3), 1735–1744 (2023)
- [38] Liu, J., Chen, Y., Dong, Z., Wang, S., Calinon, S., Li, M., Chen, F.: Robot cooking

- with stir-fry: Bimanual non-prehensile manipulation of semi-fluid objects. *IEEE Robotics and Automation Letters* **7**(2), 5159–5166 (2022)
- [39] Hu, S., Cao, X., Reddyhoff, T., Ding, X., Shi, X., Dini, D., deMello, A.J., Peng, Z., Wang, Z.: Pneumatic programmable superrepellent surfaces. *Droplet* **1**(1), 48–55 (2022)
- [40] Qu, X., Ma, X., Shi, B., Li, H., Zheng, L., Wang, C., Liu, Z., Fan, Y., Chen, X., Li, Z.: Refreshable braille display system based on triboelectric nanogenerator and dielectric elastomer. *Advanced Functional Materials* **31**(5), 2006612 (2021)
- [41] Bettelani, G.C., Averta, G., Catalano, M.G., Leporini, B., Bianchi, M.: Design and validation of the readable device: a single-cell electromagnetic refreshable braille display. *IEEE transactions on haptics* **13**(1), 239–245 (2020)
- [42] Haga, Y., Makishi, W., Iwami, K., Totsu, K., Nakamura, K., Esashi, M.: Dynamic Braille display using SMA coil actuator and magnetic latch. *Sensors and Actuators A: Physical* **119**(2), 316–322 (2005)
- [43] Liu, K., Hacker, F., Daraio, C.: Robotic surfaces with reversible, spatiotemporal control for shape morphing and object manipulation. *Science Robotics* **6**(53), 5116 (2021)
- [44] Johnson, B., Naris, M., Sundaram, V., Volchko, A., Ly, K., Mitchell, S., Acome, E., Kellaris, N., Keplinger, C., Correll, N., *et al.*: A multifunctional soft robotic shape display with high-speed actuation, sensing, and control. *Nature Communications* **14**(1), 4516 (2023)
- [45] Stanley, A.A., Hata, K., Okamura, A.M.: Closed-loop shape control of a haptic jamming deformable surface. In: 2016 IEEE International Conference on Robotics and Automation (ICRA), pp. 2718–2724 (2016). IEEE
- [46] Wave-Handling, Brochure, no. 54817, Festo. Accessed: Mar. 2024 (2013). https://www.festo.com/net/SupportPortal/Files/248127/Festo_WaveHandling-en.pdf
- [47] Omni Directional Sortation Brochure, Festo. Accessed: Mar. 2024 (2023). https://www.omniawheel.com/_files/ugd/71243f_320ec349b4024f30bd4b2ea87f071129.pdf
- [48] Reznik, D., Canny, J.: A flat rigid plate is a universal planar manipulator. In: Proceedings. 1998 IEEE International Conference on Robotics and Automation (Cat. No.98CH36146), vol. 2, pp. 1471–1472 (1998)
- [49] Deng, Z., Stommel, M., Xu, W.: A novel soft machine table for manipulation of delicate objects inspired by caterpillar locomotion. *IEEE/ASME Transactions on Mechatronics* **21**(3), 1702–1710 (2016)

- [50] Ruggiero, F., Petit, A., Serra, D., Satici, A.C., Cacace, J., Donaire, A., Ficuciello, F., Buonocore, L.R., Fontanelli, G.A., Lippiello, V., Villani, L., Siciliano, B.: Non-prehensile manipulation of deformable objects: Achievements and perspectives from the robotic dynamic manipulation project. *IEEE Robotics & Automation Magazine* **25**(3), 83–92 (2018)
- [51] Chen, Z., Deng, Z., Dhupia, J.S., Stommel, M., Xu, W.: Trajectory planning and tracking of multiple objects on a soft robotic table using a hierarchical search on time-varying potential fields. *IEEE Transactions on Robotics* **40**, 351–363 (2024)
- [52] Canfield, S.L., Reinholtz, C.F.: Development of the carpal robotic wrist. In: Casals, A., Almeida, A.T. (eds.) *Experimental Robotics V*, pp. 423–434. Springer, Berlin, Heidelberg (1998)
- [53] Mintchev, S., Salerno, M., Cherpillod, A., Scaduto, S., Paik, J.: A portable three-degrees-of-freedom force feedback origami robot for human–robot interactions. *Nature Machine Intelligence* **1**(12), 584–593 (2019)
- [54] Mete, M., Paik, J.: Closed-Loop Position Control of a Self-Sensing 3-DoF Origami Module With Pneumatic Actuators. *IEEE Robotics and Automation Letters* **6**(4), 8213–8220 (2021)
- [55] Robertson, M.A., Kara, O.C., Paik, J.: Soft pneumatic actuator-driven origami-inspired modular robotic “pneumagami”. *The International Journal of Robotics Research* **40**(1), 72–85 (2021)
- [56] Huang, H., Gan, J., Zeng, C., Yang, C.: Motion regulation for single-leader-dual-follower teleoperation in flipping manipulation. In: Liu, H., Yin, Z., Liu, L., Jiang, L., Gu, G., Wu, X., Ren, W. (eds.) *Intelligent Robotics and Applications*, pp. 483–495. Springer, Cham (2022)
- [57] Huang, H., Zeng, C., Cheng, L., Yang, C.: Toward generalizable robotic dual-arm flipping manipulation. *IEEE Transactions on Industrial Electronics* **71**(5), 4954–4962 (2024) <https://doi.org/10.1109/TIE.2023.3288189>
- [58] Kuffner, J., Xiao, J.: Motion for manipulation tasks. *Springer Handbook of Robotics*, 897–930 (2016)
- [59] Kim, U., Jung, D., Jeong, H., Park, J., Jung, H.-M., Cheong, J., Choi, H.R., Do, H., Park, C.: Integrated linkage-driven dexterous anthropomorphic robotic hand. *Nature communications* **12**(1), 1–13 (2021)
- [60] Chen, T., Tippur, M., Wu, S., Kumar, V., Adelson, E., Agrawal, P.: Visual dexterity: In-hand reorientation of novel and complex object shapes. *Science Robotics* **8**(84), 9244 (2023)

- [61] Sanchez, J., Corrales, J.-A., Bouzgarrou, B.-C., Mezouar, Y.: Robotic manipulation and sensing of deformable objects in domestic and industrial applications: a survey. *The International Journal of Robotics Research* **37**(7), 688–716 (2018) <https://doi.org/10.1177/0278364918779698>
- [62] Nguyen, H.G., Kuhn, M., Franke, J.: Manufacturing automation for automotive wiring harnesses. *Procedia CIRP* **97**, 379–384 (2021) <https://doi.org/10.1016/j.procir.2020.05.254> . 8th CIRP Conference of Assembly Technology and Systems
- [63] Satici, A.C., Ruggiero, F., Lippiello, V., Siciliano, B.: A coordinate-free framework for robotic pizza tossing and catching. In: *Robot Dynamic Manipulation: Perception of Deformable Objects and Nonprehensile Manipulation Control*, pp. 207–227. Springer, Cham (2022)
- [64] Schmidgall, S., Kim, J.W., Kuntz, A., Ghazi, A.E., Krieger, A.: General-purpose foundation models for increased autonomy in robot-assisted surgery. *Nature Machine Intelligence*, 1–9 (2024)
- [65] Zhang, F., Demiris, Y.: Learning garment manipulation policies toward robot-assisted dressing. *Science Robotics* **7**(65), 6010 (2022) <https://doi.org/10.1126/scirobotics.abm6010> <https://www.science.org/doi/pdf/10.1126/scirobotics.abm6010>
- [66] Yin, H., Varava, A., Kragic, D.: Modeling, learning, perception, and control methods for deformable object manipulation. *Science Robotics* **6**(54), 8803 (2021)
- [67] Baines, R., Zuliani, F., Chennoufi, N., Joshi, S., Kramer-Bottiglio, R., Paik, J.: Multi-modal deformation and temperature sensing for context-sensitive machines. *nature communications* **14**(1), 7499 (2023)
- [68] Zhang, K., Qiu, C., Dai, J.S.: An extensible continuum robot with integrated origami parallel modules. *Journal of Mechanisms and Robotics* **8**(3), 31010 (2016)
- [69] Salerno, M., Zhang, K., Menciassi, A., Dai, J.S.: A novel 4-DOF origami grasper with an SMA-actuation system for minimally invasive surgery. *IEEE Transactions on Robotics* **32**(3), 484–498 (2016)

Supplementary material

- **Method S1.** Single Module System Modeling.
- **Method S2.** Spherical Coordinate-based Workspace Evaluation.
- **Method S3.** Multi-module Transfer Strategy.
- **Table S1.** Notation for kinematics analysis.
- **Algorithm S1.** Multi-module transition: Translate object from Surface 2 to 1.
- **Figure S1.** Module design and workspace analysis.
- **Figure S2.** Workspace analysis in spherical coordinates.
- **Movie S1.** Overview of surface-based manipulation.
- **Movie S2.** Validation of translation strategy with randomly shaped objects. A piece of randomly shaped putty is placed at different initial positions on the surface and translated to a designated target location in the upper-left corner. Six consecutive experiments were conducted, each starting from a different initial condition, to illustrate the performance of the translation strategy.
- **Movie S3.** Validation of flipping strategy. The object initially placed at a random position on the surface, is translated to the space between two planes to perform a flipping task. This sequence is executed automatically and repeated two times, demonstrating the robustness and reliability of the flipping strategy.
- **Movie S4.** Validation of rotation strategy. The object is rotated about its Z-axis to multiple target angles (20°, 30°, 60°, and 80°) in sequence. After achieving each target orientation, the system briefly maintains the object’s angle before proceeding to the next reference angle.
- **Movie S5.** Shape manipulation of free-form objects. A long strip of putty undergoes two successive folds by combining multiple previously introduced manipulation strategies.

Method S1: Single Module System Modeling

We adopted a modular design that consists of identical units. Modeling a single module allows us to understand the workspace of each unit and optimize their control to accomplish manipulation tasks. Developing an analytical model for a single module also facilitates scalability in both size and number of modules, making it easier to design larger systems or integrate additional modules as needed. To understand the relationship between the end-effector position and the joint input angles, we studied the system’s kinematics. Our structure is based on an origami-inspired Canfield mechanism [52], whose kinematics have been explored in previous studies [54, 68, 69]. To accurately represent the kinematic equations of the structure illustrated in Figure S1(a), we provided a schematic representation in Figure S1(b). Notably, the water bomb component of the leg in Figure S1(a) functions as a spherical joint within a certain range of motion. Each physical parameter in the schematic is detailed in Table S1.

Table S1 Notation for kinematics analysis

Notion	Description
$O_R \in \mathbb{R}^3$	Geometric center of the top surface
$R_i \in \mathbb{R}^3$	Revolute joint connecting the leg and the top surface
$M_i \in \mathbb{R}^3$	The midpoint of each origami leg
$O_M \in \mathbb{R}^3$	The center of the virtual plane formed by M_1, M_2, M_3
$B_i \in \mathbb{R}^3$	Revolute joint connecting the leg and the base surface
$O_B \in \mathbb{R}^3$	Geometric center of the base surface
$\theta_i \in \mathbb{R}^3$	The angle between the leg and the base plane
$l \in \mathbb{R}$	The length of $M_i B_i$, where $M_i B_i = M_i R_i$
$r \in \mathbb{R}$	The length of $O_B B_i$, where $O_B B_1 = O_B B_2 = O_B B_3$
$\phi_i \in \mathbb{R}$	The leg's azimuth angle. $\phi_1 = 0, \phi_2 = \frac{2\pi}{3}, \phi_3 = \frac{4\pi}{3}$

Forward Kinematics

To understand the relationship between the joint angles and the position and orientation of the end effector, and thereby determine its workspace, we studied the system's forward kinematics.

Assuming $O_B = [0, 0, 0]^T$ as the origin of the world coordinate system, the geometric configuration allows us to compute the coordinates of the midpoint M_i of each leg based on the input angles of the legs θ_i :

$$M_i = \begin{bmatrix} \cos\phi_i(r + l\cos\theta_i) \\ \sin\phi_i(r + l\cos\theta_i) \\ l\sin\theta_i \end{bmatrix}, \quad (1)$$

where ϕ_i represents the leg's azimuth angle, we can assume $\phi_1 = 0, \phi_2 = \frac{2\pi}{3}, \phi_3 = \frac{4\pi}{3}$.

Then, utilizing the algorithm described in [54], we can obtain the analytical solution for the Cartesian coordinates of the center of the top surface O_R .

By substituting the actual parameters $l = 5.9\text{cm}$, $r = 4.4\text{cm}$, and constraining θ_i within the range of $[30^\circ, 90^\circ]$, we can map out the workspace of the top plane in the Cartesian coordinate system as in Fig. S1(c). Here, the points's positions represent all possible coordinates of the top plane's center, with the highest center point reaching approximately 11.8cm and the lowest at about 5.9cm . Due to the distinctiveness of the Canfield structure, this parallel mechanism is a 3 DoF pointing system. As such, when the X and Y coordinates of the center of the upper surface change, the tilt angle of the upper surface also varies [69]. Therefore, for our application, unlike the current studies [54, 69] pertaining to continuum robots, knowing the center position of the plane only is insufficient. To manipulate objects through the deformation of a surface composed of multiple modules, it is crucial for us to comprehend the relationship between the tilt angle of the end effector and the input leg angles. For this, we first calculate the normal vector of the virtual plane $M_1 M_2 M_3$:

$$N = [N_x, N_y, N_z] = (M_1 - M_2) \times (M_1 - M_3). \quad (2)$$

Since the top plane R and the base plane B are symmetrical with respect to the virtual plane M [69], we can determine the representation of the normal vector of the top plane in the spherical coordinate system. Here, ψ denotes the polar angle between the

normal vector of the top plane and the positive Z-axis, and δ signifies the azimuthal angle between the normal vector and the positive X-axis:

$$\begin{aligned}\psi &= 2\arccos\left(\frac{N_z}{\sqrt{N_x^2 + N_y^2 + N_z^2}}\right), \\ \delta &= \arctan\left(\frac{N_y}{N_x}\right).\end{aligned}\tag{3}$$

Inverse Kinematics

In the design shown in Fig. S1, the three motors that can perform closed-loop position control are abstracted as nodes B_i in Fig. S1(b), with the θ representing the motor output angle. To facilitate the control of the robot for more complex closed-loop interactive behaviors in the task space, we need to understand the relationship between specific plane poses and the motor output angles. Therefore, we conducted a study on the inverse kinematics of the robot.

When describing the pose of the top square plane, we use the roll and pitch from XYZ-Euler angles (since the mechanism lacks the yaw DoF in XYZ-Euler angles) and the distance from the plane center to the base to characterize the plane's distance, which could be noted as $[Roll, Pitch, H]$. In Equation (6), we explore how to convert XYZ-Euler angles into the representation of the top plane's normal vector in spherical coordinates. In this chapter, we will focus on discussing how to determine the motor angles corresponding to $[\delta_{top}, \psi_{top}, H]$. Since the top plane of the Canfield structure is symmetrical to the bottom plane about a central virtual plane, we can obtain the representation of the inclination angle of the normal vector of the virtual plane $M_1M_2M_3$ in spherical coordinates:

$$\begin{aligned}\psi_{virtual} &= \frac{\psi_{top}}{2}, \\ \delta_{virtual} &= \delta_{top}.\end{aligned}\tag{4}$$

The distance r_0 from the center of the base to the top is:

$$r_0 = \frac{H}{\sin(\frac{\pi}{2} - \psi_{virtual})}.\tag{5}$$

Finally, according to [54] desired legs angle θ_i could be derived from this second-order polynomial equation:

$$\theta_i = 2\arctan(t_i), \theta_i \in [0, \frac{\pi}{2}],\tag{6}$$

where:

$$t_i = \frac{-b_i \pm \sqrt{b_i^2 - 4a_i c_i}}{2a_i},\tag{7}$$

$$\begin{aligned}
a_i &= (r - l)(\sin(\psi_{virtual})\cos(\delta_{virtual} - \theta_i)) - \frac{r_0}{2}, \\
b_i &= 2l\cos(\psi_{virtual}), \\
c_i &= (r + l)(\sin(\psi_{virtual})\cos(\delta_{virtual} - \theta_i)) - \frac{r_0}{2}.
\end{aligned} \tag{8}$$

Dynamics

To optimize the manipulation capabilities of our system, it is crucial to understand how the robot's end effector exerts forces at different positions within its workspace under static conditions. Analyzing the variation in the maximum external force output allows us to select the most appropriate operational workspace for manipulation tasks. We then model the robot's equations of motion (EoM) using projected Newton-Euler (PNE):

$$M(q)\ddot{q} + b(q, \dot{q}) + g(q) = \tau + J_P^T F \tag{9}$$

Where q represents the three motor angles, $M(q)$ is the mass matrix, $b(q, \dot{q})$ is the coriolis and centrifugal terms, $g(q)$ is gravitational terms, τ is the generalized torques of generalized coordinates, F is the external force acting on the top surface, and J_P is the translational Jacobian of the top plane's geometric center.

The calculation of translational Jacobian J can be obtained by taking the partial derivative for the leg joint angle, based on the relationship between the planar center position $O_R \in \mathbb{R}^3$ and the motor angle $\theta \in \mathbb{R}^3$ in the forward kinematics equation.

$$J_P = \frac{\partial O_R(\theta)}{\partial \theta} \in \mathbb{R}^{3 \times 3} \tag{10}$$

When we consider a steady-state situation, i.e. $\dot{q}, \ddot{q} = 0$, to analyze the variation of the maximum force output by the robot at different positions, we assume that the three motors always output their maximum torque. Then, using Equation (9), we can calculate the maximum external force F that the robot can hold.

In Fig. S1c, different colors represent the variation in normalized output force in the Z-axis direction at different positions, when the torque output by the three motors is always the same. Here, red represents the maximum output force, while blue indicates the minimum output force. This visualization reflects how the robot's maximum load-bearing capacity changes with the position of the top surface. Overall, the conclusion is that the load-bearing capacity is greater at higher planar heights compared to lower positions.

Method S2: Spherical Coordinate-based Workspace Evaluation

Besides the XYZ-Coordinates of the center O_R of the top plane, the spatial pose of the top plane can also be expressed as $[\psi, \delta, OR_Z]$, where OR_Z refer to the height of the plane. When the input angles of the three legs fall within the $[30^\circ, 90^\circ]$ range, we can plot the maximum tilt angles of the top plane at different heights pointing in different directions, as shown in Fig. S2. The blue dots in the Fig. S2 illustrate the possible tilt angles of the plane in various directions when the height of the plane center is within the range of different heights. The azimuthal angle in polar coordinates represents the

tilt direction of the plane’s normal vector, while the radial coordinate signifies the tilt angle of the directional vector in that direction. We can observe that the tilt angle of the plane can reach up to 46° in specific directions and when the height of the center of the surface is 8cm . When the height is between 8cm to 10cm , the maximum tilt angle of the plane in various directions appears to be relatively uniform.

Method S3: Multi-module Transfer Strategy

In Chapter 4.4, we discussed the strategy for object translation using a single module. This section extends the discussion to multi-module systems by detailing the strategies required for inter-module object translation. The basis of this approach lies in the coordinated lowering of Surface 1 while the object is on Surface 2. The transition of the object between the module surfaces is achieved by leveraging transfer strategy with Surface 2 until it securely lands on Surface 1. This process involves carefully balancing positioning, timing, and movement control to ensure stable translation of the object (see Algorithm S1). Key to this strategy is the real-time adjustment and monitoring of both modules to facilitate a smooth transition, setting the stage for subsequent transfers and maintaining the system’s readiness for ongoing operations.

Algorithm S1 Multi-module Translation: Translate object from Surface 2 to 1

```

1: procedure MULTI-MODULE TRANSLATION:  $(X_{1ref}, Y_{1ref})$ 
2:   # Line 4-5: While on surface2, surface1 tilts and lowers as surface2
   translates, guiding the object onto surface1.
3:   if  $(x, y)$  in surface1 then
4:     Surface1  $\leftarrow [0, -\theta_\beta, H_{init} - 1]$ 
5:     Surface2  $\leftarrow translation(X_{2ref}, Y_{2ref})$   $\triangleright$  Algorithm1
6:   else
7:     # Line 8-9: Once the object fully moves to surface1, execute the single-
   module transition algorithm, and reset surface2.
8:     Surface2  $\leftarrow [0, 0, H_{init}]$ 
9:     Surface1  $\leftarrow translation(X_{1ref}, Y_{1ref})$   $\triangleright$  Algorithm1
10:  end if
11: end procedure

```

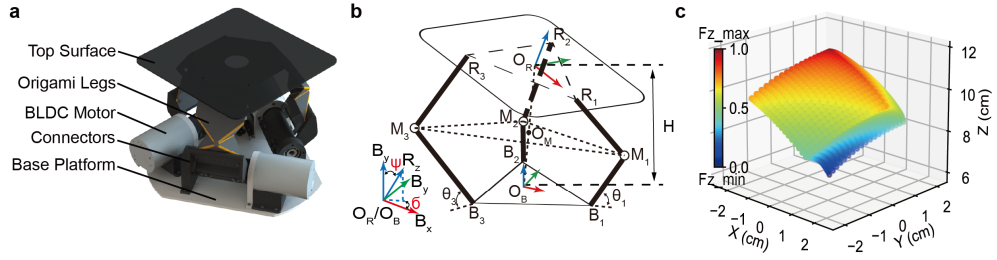


Fig. S1 Module design and workspace analysis. (a) Module design. Each module consists of an acrylic top surface, origami-based legs fabricated from FR4 and polyimide layers, BLDC motors for actuation, PLA connectors, and an acrylic base platform. (b) Robot structural schematic. (c) Cartesian analysis: $\theta \in [30^\circ, 90^\circ]$. Dots highlight viable center positions. Different colors represent the variation in normalized output force in the Z-axis direction at different positions while maintaining uniform torque outputs across the three motors. Here, red represents the maximum output force, while blue indicates the minimum output force.

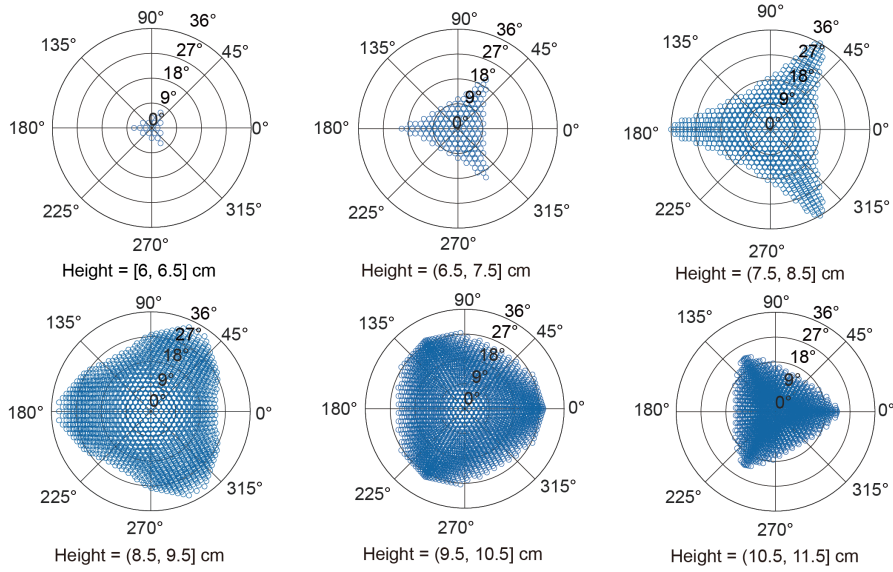


Fig. S2 Workspace analysis in spherical coordinates. The maximum tiltable angle changes with elevation and direction. In the polar plots, azimuth signifies tilt direction, and radius quantifies potential tilt based on set conditions. The tilt corresponds to the plane's normal vector in spherical coordinates.